Fast left ventricle tracking using localized anatomical affine optical flow

Sandro Queirós[1,2,3*], João L. Vilaça[1,4], Pedro Morais[1,2,5], Jaime C. Fonseca[3], Jan D'hooge[2], Daniel Barbosa[1]

[1]*ICVS/3B's - PT Government Associate Laboratory, Braga/Guimarães, Portugal*

[2]*Lab on Cardiovascular Imaging and Dynamics, Dept. of Cardiovascular Sciences, KU Leuven, Leuven, Belgium*

[3]*Algoritmi Center, School of Engineering, University of Minho, Guimarães, Portugal*

[4]*DIGARC - Polytechnic Institute of Cávado and Ave (IPCA), Barcelos, Portugal*

[5]*INEGI, Faculty of Engineering, University of Porto, Porto, Portugal*

SUMMARY

In daily clinical cardiology practice, left ventricle (LV) global and regional function assessment is crucial for disease diagnosis, therapy selection and patient follow-up. Currently, this is still a time-consuming task, spending valuable human resources. In this work, a novel fast methodology for automatic LV tracking is proposed based on localized anatomically constrained affine optical flow. This novel method can be combined to previously proposed segmentation frameworks or manually delineated surfaces at an initial frame to obtain fully delineated datasets and, thus, assess both global and regional myocardial function. Its feasibility and accuracy was investigated in three distinct public databases, namely in realistically simulated 3D ultrasound (US), clinical 3D echocardiography and clinical cine cardiac magnetic resonance (CMR) images. The method showed accurate tracking results in all databases, proving its applicability and accuracy for myocardial function assessment. Moreover, when combined to previous state-of-the-art segmentation frameworks, it outperformed previous tracking strategies in both 3D US and CMR data, automatically computing relevant cardiac indices with smaller biases and narrower limits of agreement compared to reference indices. Simultaneously, the proposed localized tracking method showed to be suitable for online processing, even for 3D motion assessment. Importantly, although here evaluated for LV tracking only, this novel methodology is applicable for tracking of other target structures with minimal adaptations.

Received . . .

*Correspondence to: Sandro Queirós, Life and Health Sciences Research Institute (ICVS), Universidade do Minho, Campus de Gualtar, 4710-057 Braga, Portugal. Email: sandroqueiros@med.uminho.pt

This article has been accepted for publication and undergone full peer review but has not been through the copyediting, typesetting, pagination and proofreading process, which may lead to differences between this version and the Version of Record. Please cite this article as Int. J. Numer. Meth. Biomed. Engng., e02871. doi: 10.1002/cnm.2871

KEY WORDS: localized affine optical flow; fast image processing; left ventricle tracking; automatic quantification; cardiac cine MRI; 3D echocardiography

1. INTRODUCTION

In cardiology practice, accurate assessment of cardiac performance is clinically important for patient management, disease diagnosis, risk stratification or therapy selection [1, 2, 3]. Noninvasive imaging has a key role in such daily examination, with numerous modalities (e.g., cardiac magnetic resonance (CMR) imaging, 2D and 3D echocardiography or computed tomography) currently being used in the context of different cardiovascular diseases. Specifically, left ventricle (LV) morphology and function assessment by noninvasive imaging is a crucial part of daily routine [1, 2, 3, 4]. A comprehensive analysis includes the evaluation of both global and regional LV function. While the former includes the computation of several clinical cardiac indices, namely end-diastolic volume (EDV), end-systolic volume (ESV), stroke volume (SV), LV mass (LVM) and ejection fraction (EF) [5], the latter focuses on a more localized assessment, namely motion/strain analysis [6]. Their extraction comprehends manual or semi-automatic processes [6, 7], such as the complete delineation of the LV, therefore requiring valuable human resources.

To ease these analyses, continuous efforts from the research community and medical vendors have been made during the last decades. Indeed, several (semi-)automated segmentation frameworks have been proposed to delineate the inner and/or outer border of the myocardium in different modalities [7, 8], enabling the computation of the relevant cardiac indices. These methodologies include, among others, image-based techniques [9], deformable models [10, 11, 12, 13, 14, 15, 16], graph cuts [17], active shape and appearance models [18, 19, 20, 21], atlas-based methods [22, 23, 24] or machine learning strategies [25, 26, 27]. Since multiple cardiac phases need to be analyzed for a comprehensive analysis, either sequential segmentation (segmentation at time t used at time $t+1$) or tracking are then usually applied. The former focuses on identifying the target structure on consecutive frames, using specific temporal priors added to the mathematical formulation [11, 12]. The latter focuses on following the motion of specific patterns along the cardiac sequence, thus allowing to extract the motion and deformation of the target structure [6]. Tracking methodologies include techniques based on block matching [28], non-rigid registration [29, 30, 31, 32, 33], optical flow [16, 34, 35, 36, 37], deformable models [38], among others [39, 40]. These methods differ on the way the motion is estimated over the image sequence, presenting different computational burdens and accuracies according to the modality and specific application [41]. While typically sequential segmentation strategies allow to compute global LV function only, tracking methodologies may also

permit to assess regional myocardial motion and deformation, assessing strain measures and easing the detection of ischemia, infarction or dyssynchrony [6, 42].

Focusing on automating LV global function analysis in both 3D echocardiography and CMR data, our team has recently proposed two frameworks for fast 3D+time LV segmentation [16, 34]. Both methodologies automatically segment the left ventricle at the end-diastole (ED) frame by adapting the recent B-spline Explicit Active Surfaces (BEAS) framework [43] according to the specific requirements and image challenges of the corresponding modality. Then, a global anatomically constrained affine optical flow tracking (henceforth named global AAOF) was used to track the ED LV surface throughout the cardiac cycle, ultimately assessing the LV morphology at the end-systole (ES) frame. While these frameworks presented highly competitive results against state-of-the-art methods and excellent agreements with reference cardiac indices [16, 34], their tracking module was found to be the least performing one [44, 45]. Indeed, by propagating the LV boundaries assuming a global affine motion model between adjacent frames, the tracking module has the ability to follow a multitude of motion patterns with spatially consistent shapes but has difficulties in following local motion or deformation inhomogeneity of the myocardial wall (e.g., cases of ischemia or infarction). Focusing on mitigating this issue, Barbosa *et al.* [45] recently proposed a novel tracking method, combining the original global anatomically constrained affine optical flow strategy with a local refinement scheme based on block matching. The latter allows to increase the degrees of freedom of the estimated motion model, increasing the realism of the obtained LV shape and presenting more complex deformation patterns with local variations. Nonetheless, being locally refined, the method is intrinsically more sensitive to image artifacts and errors. Although the abovementioned limitations can have a limited impact on global LV function analysis (as the global tracker is robust for surface-based propagation), it prevents the use of these frameworks for regional function assessment.

In this work, the main contributions are threefold:

- First, we propose a fast and automatic LV tracking methodology based on localized anatomically constrained affine optical flow (henceforth named localized AAOF). This method can be combined to previously proposed segmentation strategies (e.g., Barbosa *et al.* [45], Queirós *et al.* [16]) or manually delineated surfaces at the ED frame to obtain complete delineated datasets and, thus, assess both global and regional myocardial function. Note that a preliminary 2D formulation of this novel methodology was previously presented in [44]. Hereto, its application towards 3D data and associated mathematical formalism is detailed.
- Secondly, we evaluate its accuracy for global and regional myocardial function assessment within an *in-silico* experimental setup. In this sense, realistically simulated 3D ultrasound (US) sequences, and corresponding ground truth 3D motion fields, are used for validation.

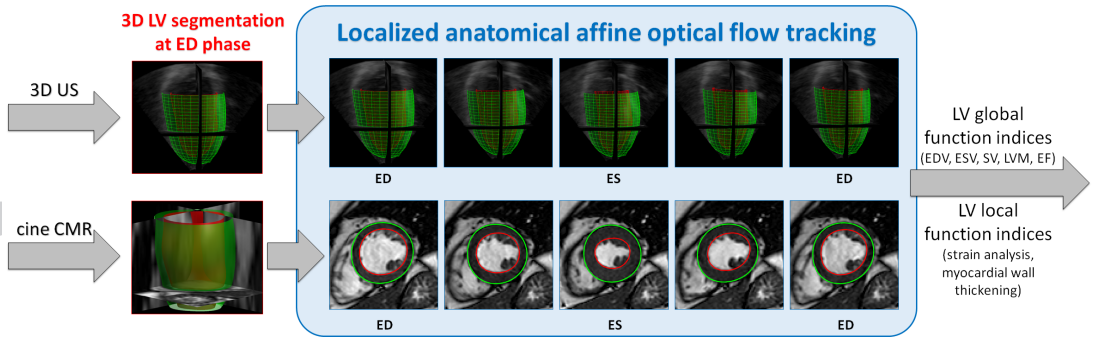

Figure 1. Overview of the proposed localized anatomically constrained affine optical flow.

Moreover, the method's sensitivity to parameter settings is also investigated, providing further insights into its performance.

- Lastly, we corroborate its applicability to multiple imaging modalities in real clinical data. To this end, the algorithm's accuracy is assessed in two distinct databases: (1) 30 clinical 3D echocardiography sequences; and (2) 45 3D+t cine CMR datasets (stack of 2D+t slices).

This paper is structured as follows. In Section 2, we focus on the proposed tracking methodology, starting from its global counterpart and then modified towards localized motion estimation. Section 3 presents the validation experiments and results in three distinct public databases. In Section 4, we evaluate and discuss the algorithm's performance and compare with its global counterpart and state-of-the-art methods. Finally, the main conclusions are given in Section 5.

2. METHODS

2.1. Overview

Starting from the delineated LV surface (usually at the ED frame), the principle is to estimate the motion between adjacent frames using optical flow. In order to reduce its computational burden and avoid the influence of surrounding tissues, we propose to anatomically constrain the motion estimation step by only considering a region of interest (ROI) around the tracked surface. Subsequently, the estimated motion is integrated into an affine motion model (global/local model for global/localized tracking). In the end, relevant global cardiac indices and local myocardial function parameters can be extracted from the automatically tracked surfaces (Figure 1).

Note that, in order to better understand the mathematical formalism behind the proposed localized AAOF, its 3D global counterpart (global AAOF, proposed in [34] and [16]) is first presented and then extended towards local motion assessment.

2.2. *Global anatomical affine optical flow*

The optical flow algorithm relies on the well-known brightness constancy assumption [46], which presupposes that the intensity of a particular point in a moving pattern does not change over time. This implies that any difference in the local appearance of a region over a temporal sequence is uniquely defined by its underlying motion. Let $I(\boldsymbol{x}, t)$ denote the pixel intensity at location $\boldsymbol{x} = [x_1, x_2, x_3]$ and time t in a given 4D image dataset. Based on the least square solution of the optical flow equation [46] and taking the affine motion model as defined in [47], the underlying 3D affine motion can be estimated by minimizing the following energy:

$$E_g = \int_{\mathbb{R}^3} \mathcal{W}(x_1 - r_1, x_2 - r_2, x_3 - r_3)(I_1 u + I_2 v + I_3 w + I_t)^2 \, d\boldsymbol{x}, \tag{1}$$

where

$$u(x_1, x_2, x_3) = u_0 + u_1(x_1 - r_1) + u_2(x_2 - r_2) + u_3(x_3 - r_3), \tag{2}$$

$$v(x_1, x_2, x_3) = v_0 + v_1(x_1 - r_1) + v_2(x_2 - r_2) + v_3(x_3 - r_3), \tag{3}$$

$$w(x_1, x_2, x_3) = w_0 + w_1(x_1 - r_1) + w_2(x_2 - r_2) + w_3(x_3 - r_3), \tag{4}$$

encode the local motion field along x_1, x_2 and x_3, respectively. $\mathcal{W}$ is a window function defining the ROI where the chosen motion model is assumed to be constant. $\boldsymbol{r} = [r_1, r_2, r_3]$ is the position to which the estimated motion is referenced (in the current implementation, $\boldsymbol{r} = [0, 0, 0]$). $\boldsymbol{\nabla I} = [I_1, I_2, I_3]$ is the local image spatial gradient, whereas I_t is the temporal derivative. In order to reduce noise sensitivity during spatial gradient assessment, $\boldsymbol{\nabla I}(\boldsymbol{x})$ is computed using Gaussian derivative kernels along each direction. I_t is simply computed with finite forward differences.

From the estimated motion field, the affine transformation that describes the motion between adjacent frames can be written as the augmented matrix:

$$A = \begin{bmatrix} 1 + u_1 & u_2 & u_3 & u_0 \\ v_1 & 1 + v_2 & v_3 & v_0 \\ w_1 & w_2 & 1 + w_3 & w_0 \\ 0 & 0 & 0 & 1 \end{bmatrix}. \tag{5}$$

As originally proposed in [34], and contrarily to traditional optical flow strategies which compute the motion across a pre-defined regular region [47], the motion estimation is confined to an anatomical ROI. To this end, the method takes advantage of the fact that the surface to be tracked is known at the initial temporal phase, defining the window function with respect to such anatomical ROI. Besides reducing the method's computational time, the constrained estimation preserves the

constant motion assumption over the defined region by avoiding the influence of surrounding tissues (e.g., left/right ventricles' blood pools, atria, pericardium). Hence, $\mathcal{W}$ is given by:

$$\mathcal{W}(\boldsymbol{x}) = \sum_{\boldsymbol{x}_k \in \Gamma} \mathcal{N}(\boldsymbol{x}_k), \tag{6}$$

where $\mathcal{N}(\boldsymbol{x})$ is a neighborhood function defined as a 3D binary cube of size n_{nhood} mm centered in $\boldsymbol{x}$ (see Figure 2A) and $\boldsymbol{x}_k \in \Gamma$ stands for the sampled points on the surface Γ being tracked. Note that the window size controls the amount of surface's neighbor region used to estimate the motion, thus being a paramount parameter to be defined according to the application and chosen modality. Motion of surrounding tissues may influence the estimated motion if a large window is chosen, while a small one may not be sufficient to capture enough information to estimate the true underlying motion.

Since differential optical flow approaches are best suited to estimate small displacements, an iterative displacement refinement scheme is applied [16, 34]. Hereto, the estimation step is iteratively applied, progressively accumulating the estimated displacement fields and warping the target image, therefore iteratively reducing the amount of motion left to be estimated. Once again, the number of iterations applied should be defined according to the application (*i.e.* based on the expected amount of motion for the object under study).

2.3. Localized anatomical affine optical flow

Contrarily to the global methodology, the proposed localized approach aims to independently estimate the motion for each surface point based on its anatomically constrained neighborhood. Let $\Gamma(\theta, \varphi)$ represent the boundary being tracked given as a function of angles θ and φ of a spherical space centered at $\boldsymbol{c} = [c_1, c_2, c_3]$. The principle of the proposed approach is to estimate the motion for each surface point based on its location $\boldsymbol{x}$, while also taking into account its spherical position, (θ, φ), in the boundary Γ. Thus, the local motion field around each surface point $\Gamma(\theta, \varphi)$ is encoded independently as:

$$u_{\theta,\varphi}(x_1, x_2, x_3) = u_{0,\theta,\varphi} + u_{1,\theta,\varphi}(x_1 - r_1) + u_{2,\theta,\varphi}(x_2 - r_2) + u_{3,\theta,\varphi}(x_3 - r_3) \tag{7}$$

$$v_{\theta,\varphi}(x_1, x_2, x_3) = v_{0,\theta,\varphi} + v_{1,\theta,\varphi}(x_1 - r_1) + v_{2,\theta,\varphi}(x_2 - r_2) + v_{3,\theta,\varphi}(x_3 - r_3) \tag{8}$$

$$w_{\theta,\varphi}(x_1, x_2, x_3) = w_{0,\theta,\varphi} + w_{1,\theta,\varphi}(x_1 - r_1) + w_{2,\theta,\varphi}(x_2 - r_2) + w_{3,\theta,\varphi}(x_3 - r_3) \tag{9}$$

which is estimated by minimizing the following energy:

$$E_{local}(\theta, \varphi) = \int_{\mathbb{R}^3} \mathcal{W}(x_1 - r_1, x_2 - r_2, x_3 - r_3, \theta, \varphi)(I_1 u_{\theta,\varphi} + I_2 v_{\theta,\varphi} + I_3 w_{\theta,\varphi} + I_t)^2 \, d\boldsymbol{x} \tag{10}$$

As in its global counterpart, the estimation is confined to an anatomical ROI given by the initial surface to be tracked and encoded by $\mathcal{W}(\boldsymbol{x}, \theta, \varphi)$. However, in opposition to the global strategy [16, 34], we propose to integrate the estimated motion into a local displacement by considering the neighboring regions and their spherical distance to the point of interest (θ and φ, measured assuming a spherical space). Therefore, the ROI is given by:

$$\mathcal{W}(\boldsymbol{x}, \theta, \varphi) = \sum_{\boldsymbol{x}_k \in \Gamma} \mathcal{N}(\boldsymbol{x}_k) \left(\frac{1}{2\pi\sigma_\theta\sigma_\varphi} e^{-\left(\frac{(\theta_k-\theta)^2}{2\sigma_\theta^2} + \frac{(\varphi_k-\varphi)^2}{2\sigma_\varphi^2} \right)} \right), \tag{11}$$

where (θ_k, φ_k) are the spherical coordinates of surface point $\boldsymbol{x}_k$. σ_θ and σ_φ are given according to the desired support for the localized estimation. These can be defined independently, thus having the possibility to control the smoothness of the estimated motion differently for each direction of the spherical space. Moreover, different coordinate spaces can be used to describe the surface being tracked and the corresponding anatomical ROI (e.g., cylindrical space - see cine CMR experiments in Section 3.3), therefore being possible to define the localized support parameters according to the anatomy being tracked. Together with the principle of the anatomically constrained estimation, these parameters give the proposed tracking approach an ability to use the tracked surface and its expected motion as anatomical priors. Note that, according to the initial surface (*i.e.* open/closed mesh) and the chosen coordinate space, the boundary conditions for the localized estimation might need to be adapted (see Section 3).

Overall, for each point in the surface, a local affine motion model is independently estimated via a weighted anatomical ROI, in opposition to the global affine motion originally estimated. These differences between both methods, and their 3D motion fields, are illustrated in Figure 2.

3. EXPERIMENTS AND RESULTS

3.1. Realistically simulated 3D echocardiography

3.1.1. Data description: Since true validation of 3D tracking methodologies is not possible using clinical data and is complex using dynamic physical phantoms, we chose to use a publicly available synthetic US database[†] to perform a first validation of the proposed approach. The synthetic database currently comprehends eight 3D sequences with available 3D ground truth motion fields, which were generated using the pipeline described in [48]. Contrarily to other synthetic datasets, this database contains very realistic image properties by combining ultrasound and electromechanical (E/M)

[†]https://team.inria.fr/asclepios/data/straus/

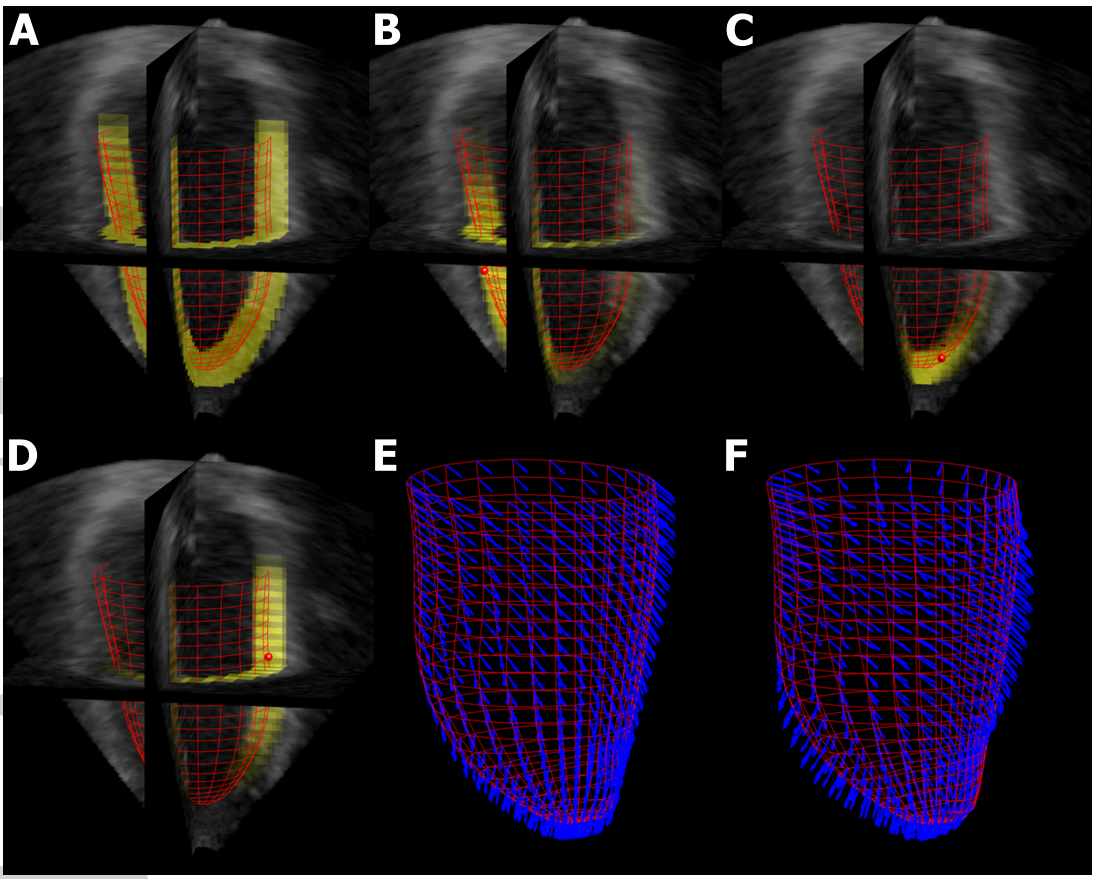

Figure 2. (A) Global and (B-D) localized AAOF at 3 different surface points (red spheres). (E) Global affine motion estimated using the entire anatomical ROI in (A). (F) Motion field estimated using the proposed localized strategy, by independently estimating the motion for each surface point. The red wireframe represents the surface being tracked, while the overlaid yellow region represents the anatomical ROI. The blue arrows represent the motion displacement estimated (E) globally and (F) locally. Note that the current figure is only a representation and the vectors are zoomed with equal factor in both situations.

simulations with a real template recording. In this way, the speckle texture of real US recordings can be learnt and combined with a myocardial motion controlled by an E/M model. As a result, these realistically simulated 3D datasets are very similar to real US acquisitions (see Figure 4), including all major elements that make motion tracking challenging: (1) motion of surrounding structures (e.g., papillary muscles and valves); (2) heterogeneities of speckle contrast inside the myocardium; and (3) speckle decorrelation over time. By varying the parameters of the E/M model, different pathophysiological conditions can be simulated. In this sense, the database includes one healthy sequence, four ischemic cases (denominated LADprox, LADdist, LCV and RCA according to the simulated artery occlusion), and three cases of dilated cardiomyopathy (denominated sync, LBBBsmall and LBBB according to the simulated activation pattern). All sequences were originally simulated with a voxel size of $0.7 \times 0.9 \times 0.6$ mm^3 and a temporal resolution of 34 frames/s, and were later resampled to $0.6 \times 0.6 \times 0.6$ mm^3. The available ground truth meshes are regularly sampled along the radial, longitudinal and circumferential directions (with 3, 30 and 25 points,

respectively), while also split into 17 segments as in the standard AHA subdivision [49]. For more details on this synthetic database, the reader is kindly referred to the original publication in [48].

3.1.2. Implementation details: For each sequence, the ground truth mesh at the ED phase was used as initial surface to be tracked throughout the cardiac cycle. Since the mesh is radially divided in 3 points, we chose to divide the myocardial mesh into three independent layers, namely endo-, mid- and epicardial surfaces, which are individually propagated by estimating their motion between adjacent frames. Since the available surfaces were cut at the LV base (Figure 4), special attention should be given to the boundary conditions applied in the proposed localized tracking strategy. Hereto, a spherical space was used, applying periodic boundaries over the θ direction, 180° shifted mirrored at the LV apex, and mirror boundaries at the basal end. Note that to ensure a single and continuous motion of the surface points at the apex (due to the singularity of the spherical space at $\varphi = -\pi$), the motion is regularized by taking their average. Moreover, in order to minimize error accumulation over time, we ensure a minimal number of propagation steps by implementing a bi-directional tracking strategy combining forward and backward estimates for half the total number of cardiac phases [16].

In this experiment, the localized support parameters along θ and φ were initially set to $\pi/3$ and $\pi/5$ rad, respectively, 4 iterations were applied in the refinement scheme and a standard deviation (SD) of 1 px was used for the Gaussian derivative kernels. Moreover, a cubic region with $\sim 9^3 mm^3$ was set for the neighborhood function.

3.1.3. Performance assessment: First, in order to tune the parameters of the proposed methodology and study the algorithm's robustness and stability, the influence of the parameters' variation on the global tracking accuracy was assessed. The global tracking accuracy was estimated by measuring the amplitude of the error vector between the 3D position of each surface point on the ground truth mesh and on the tracked result mesh, and their average and standard deviation computed over all nodes, time points and sequences. This study was performed in 2 sequences only (LADprox and LBBB), as advised by the database's organizers to avoid training over-tuning. In this sense, the 4 most relevant parameters were included in the analysis, namely the localized support parameters (σ_θ and σ_φ), the number of iterations used in the iterative displacement refinement scheme (nb_{it}), the size of the neighborhood cubic regions (n_{nhood}) and the standard deviation of the Gaussian derivative kernels (σ_{g_kernel}). The range where the parameter influence was evaluated was defined as a $\pm$ 50% variation around the abovementioned parameter values. The tracking was then applied using the new value of one parameter while keeping the remaining ones fixed to their original value. To check for differences in the average and standard deviation of the amplitude errors, unpaired t-test and F-test

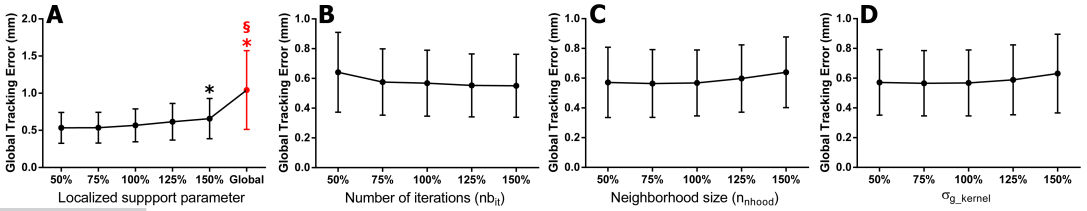

Figure 3. Influence of the variation of 4 parameters on the global tracking accuracy. (A) Localized support parameters (σ_θ, $[\pi/6; \pi/2]$ rad, σ_φ, $[\pi/10; 3\pi/10]$ rad, and global AAOF strategy); (B) number of iterations used in the iterative displacement refinement scheme (nb_{it}, $[2; 6]$); (C) size of the neighborhood cubic regions (n_{nhood}, $[6; 11]$ mm); and (D) the standard deviation of the Gaussian derivative kernels (σ_{g_kernel}), $[0.5; 1.5]$ px). $^{*}p < 0.05$, two-tailed unpaired t-test (with Welch's correction) against baseline settings. $^{\S}p < 0.05$, two-tailed F-test against baseline settings.

against the results using the baseline values were used respectively. A p-value < 0.05 was considered statistically significant.

After determining the optimal parameters for the 2 training sequences, the algorithm's performance was evaluated for both global and regional myocardial function assessment in the 8 available datasets. To this end, the global tracking accuracy was computed, while also evaluating the tracking error separately for endo-, mid- and epicardial layers. For regional function assessment, ES radial, longitudinal and circumferential strains were measured as the relative change in distance between two neighboring mesh nodes (for each direction independently). The obtained strain maps were then visually compared to ground truth ones.

The reported computational times were obtained using MATLAB code running on a Intel (R) Core (TM) i7 CPU at 2.8 GHz (shared memory of 16 GB).

3.1.4. Results: Figure 3 illustrates the influence of the variation of each parameter in the tracking performance for the 2 training sequences. To stress the added value of the localized tracking, the performance of the global AAOF approach was also added in the localized support parameters' plot. The performed sensitivity analysis reveals that the overall tracking performance is not significantly compromised within the studied range of the parameters values. The most critical choice for the overall tracking performance was found to be the localized support parameters, which control the smoothness of the estimated motion. Nonetheless, a statistically significant difference in the average error was only found for a variation of $+50\%$. When compared to the original global AAOF approach, a significant improvement was found for the proposed localized AAOF. Based on these results, the optimal parameters were then set, namely $\sigma_\theta = \pi/4$ rad, $\sigma_\varphi = 3\pi/20$ rad, $nb_{it} = 5$, $\sigma_{g\_kernel} = 0.75$ px, and $n_{nhood} \approx 7$ mm.

In the 8 sequences, the proposed localized AAOF approach presented a global tracking error of 0.54 ± 0.51 mm (5^{th} percentile, median and 95^{th} percentile of 0.08, 0.38 and 1.54 mm, respectively). When considering endo-, mid- and epicardial layers independently, the global tracking error was

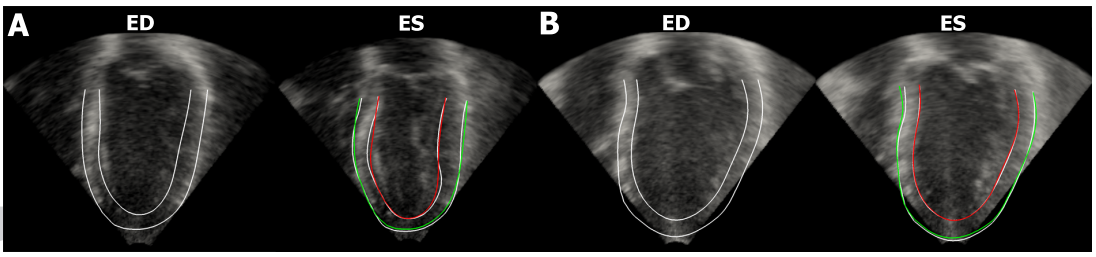

Figure 4. Tracking performance of the proposed method on both (A) LADprox and (B) LBBB simulated sequences (white: ground truth surface; red: tracked endocardial surface; green: tracked epicardial surface).

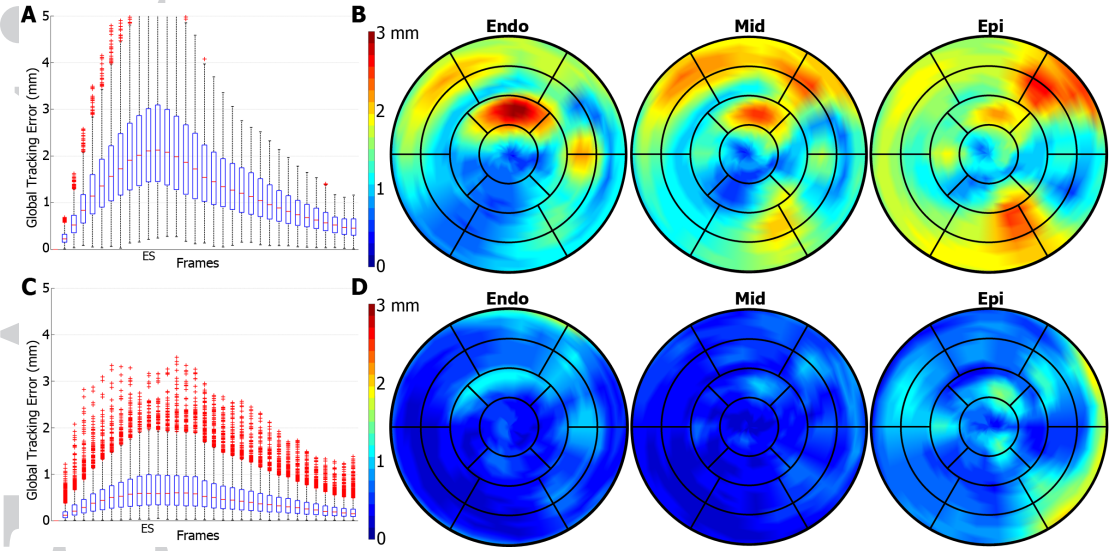

Figure 5. Boxplots of tracking error over time for the full mesh of the LADprox sequence using either the global (A) or localized (C) AAOF approach. The ends of the whiskers represent the lowest and highest data point still within 1.5 times the inter-quartile range of the lower and upper quartile, respectively. Any data value larger is considered an outlier and plotted as a red cross. (B) and (D) present the corresponding bull's eye plots of the average tracking errors' spatial distribution for the endo-, mid- and epicardial layers.

found to be 0.43 ± 0.36 ([0.08, 0.32, 1.15] mm), 0.36 ± 0.31 ([0.07, 0.27, 0.96] mm) and 0.88 ± 0.67 ([0.17, 0.69, 2.24] mm), respectively. Figure 4 shows the tracking result at the ES phase for the two training sequences. Moreover, Figure 5 presents the tracking error over time for the LADprox sequence with both global and localized AAOF approaches, together with the bull's eye plots of the errors' spatial distribution for each layer. Once again, a clear accuracy improvement was found for the proposed localized strategy. The highest errors were found to be at the ES frame (Figure 5C), which corresponds to the time point of maximum displacement. When assessing errors' spatial distribution (Figure 5D), larger errors were found at the LV base (*i.e.* outer segments of the bull's eye plots, particularly in the lateral wall), with higher emphasis on the epicardial layer.

Finally, to evaluate the performance for regional myocardial function assessment, Figure 6 presents the bull's eye plots of ES circumferential, radial and longitudinal strains for both automatically tracked (using global or localized AAOF) and ground truth meshes on the LADprox sequence. To reduce boundary effects, the strain was measured at the mid-myocardial layer. For all anatomical directions, the strain maps achieved with the automatic localized AAOF strategy

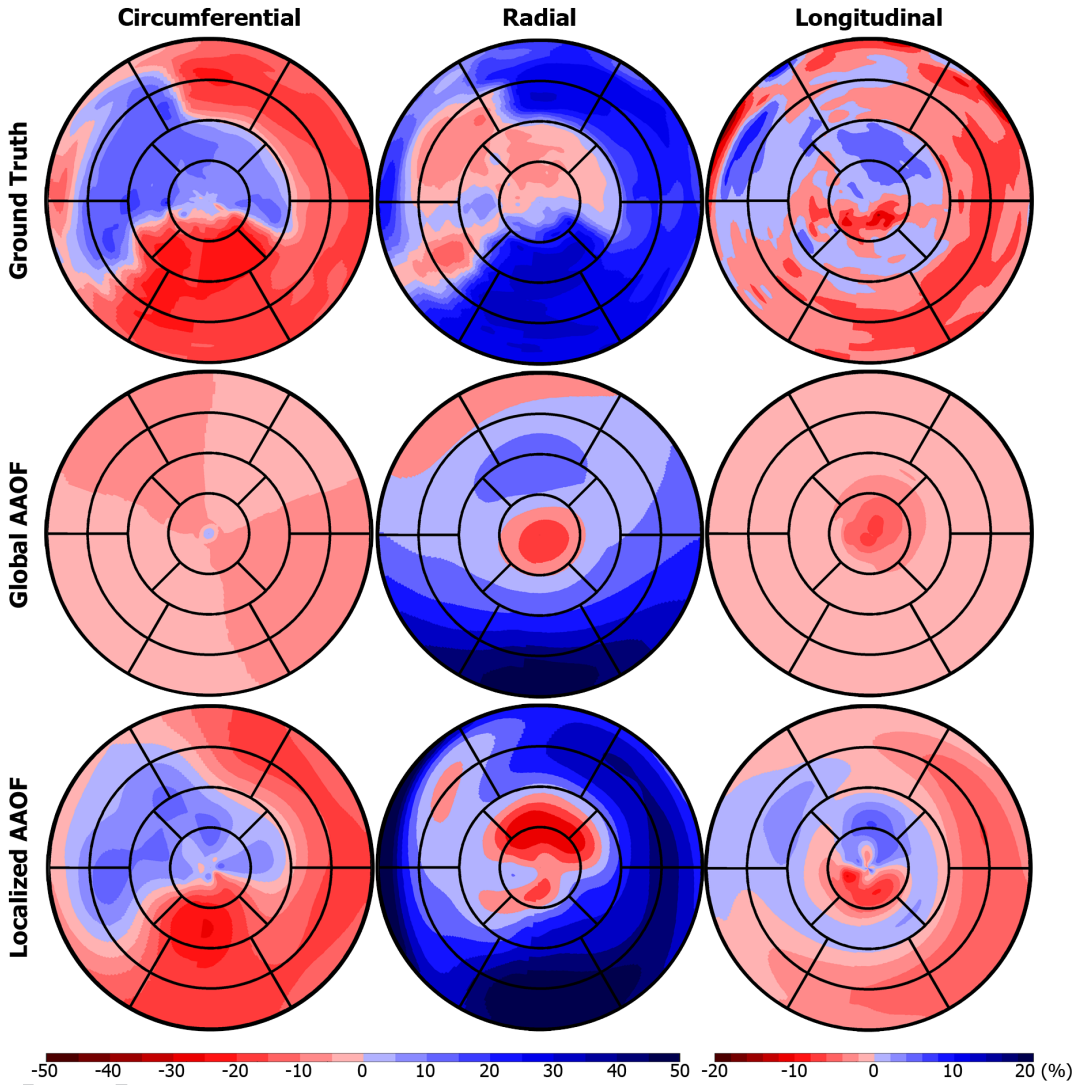

Figure 6. Bull's eye plots of ES circumferential, radial and longitudinal strain for the LADprox sequence (top: ground truth; middle: global AAOF tracking; bottom: localized AAOF tracking).

were found to be qualitatively similar to the ground truth ones. Nonetheless, circumferential strain was found to be slightly underestimated, while radial strain was overestimated. All strain maps were smoother than the corresponding reference ones. In its turn, and as initially mentioned, the global AAOF strategy was unable to assess regional function. Indeed, both circumferential and longitudinal strain maps were significantly different from the ground truth, with only the radial component showing similarities to the reference map. The latter result arises from the fact that each layer was independently tracked.

Regarding its computational burden, the proposed localized tracking methodology took, on average, 2.5 s/frame. Note that, since the 3 layers are independently propagated, a parallel MATLAB implementation was used.

3.2. Clinical 3D echocardiography

3.2.1. Data description: In order to assess the relevance of the proposed localized tracking methodology on clinical data, the database of the recent Challenge on Endocardial Three-Dimensional Ultrasound Segmentation (CETUS)[‡] was used [50]. The database includes 45 sequences of 3D echocardiography acquired at three different hospitals and with three different brands of ultrasound machines. Fifteen datasets are available as training set, with corresponding manual endocardial reference meshes at ED and ES phases publicly available. The remaining datasets correspond to the validation set and only the 3D sequences are openly available. The database's population includes 15 healthy subjects, 15 patients with previous myocardial infarction and 15 with dilated cardiomyopathy. After isotropic resampling, the datasets presented a voxel resolution from 0.6^3 mm^3 to 1.1^3 mm^3, with 13 to 47 frames. For further details regarding the CETUS data and ground truth delineations, the reader is kindly referred to [50] and [51].

3.2.2. Implementation details: In the current experiment, we propose to assess the performance of the proposed tracking methodology when combined with a previously presented LV segmentation framework for 3D US data [45]. In its original formulation, after an automatic LV segmentation at the ED phase, a two-step tracking strategy was used, combining the original global anatomically constrained affine optical flow strategy with a local refinement scheme based on block matching. Hereto, we propose to use the LV surface at the ED phase obtained using the automatic LV segmentation framework originally proposed in [45], while replacing their tracking module with our proposed localized AAOF. Note that, since closed surfaces are obtained at the ED time point, a spherical space was assumed with a periodic boundary over the θ direction and $180°$ shifted mirroring at both LV apex and base.

For the present database, the localized support parameters along θ and φ were, respectively, set to $3\pi/4$ and $\pi/4$ rad. Although the same number of neighboring regions were used, their support differ due to the different sampling of the ED LV surface (obtained with the automatic segmentation strategy) in both directions of the spherical space. Moreover, 5 iterations were considered in the refinement scheme. Finally, a SD of 1 px was used for the Gaussian derivative kernels, while a cubic region of $\sim 9^3 mm^3$, was considered for the neighborhood function.

3.2.3. Performance assessment: In order to assess the performance of the tracking alone, the 15 training datasets were used. Since the ED reference surface is known for these cases, the algorithm

[‡]https://miccai.creatis.insa-lyon.fr/miccai/

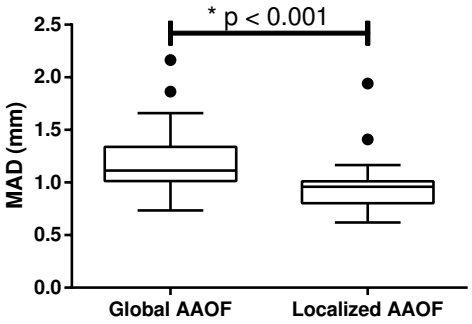

Figure 7. Tracking performance on the 15 training datasets using the global and localized AAOF approaches, assessed at the ES moment only. * two-tailed paired t-test between approaches.

was applied to track the LV until the ES moment, with the final ES tracked surface being assessed using the average point-to-surface distance towards the reference one.

Moreover, the performance of the segmentation plus tracking framework was assessed using distance metrics to the reference manually delineated surfaces, namely mean absolute distance (MAD), Hausdorff distance (HD) and Dice coefficient (Dice). These metrics were computed directly through the challenge MIDAS platform[‡] for the 30 datasets of the validation set. The accuracy of the estimated LV cardiac indices, namely EDV, ESV and EF, was equally assessed through comparison against reference indices. To this end, Pearson's correlation coefficient (R) and Bland-Altman [52] limits of agreement (LOA) between ground truth and automatically estimated LV indices were computed.

3.2.4. Results: Figure 7 presents the tracking performance on the 15 training datasets, when starting with the ED reference surface. While the localized AAOF obtained a MAD error of 1.01±0.31 mm, its global counterpart showed an error of 1.22±0.38 mm. As reported in the *in silico* experiments, the localized approach had a statistically significant higher accuracy over the global strategy.

Table I and Table II summarize the overall segmentation plus tracking performance for the 30 validation datasets (together with state-of-the-art approaches). The result for the original global anatomically constrained affine optical flow alone (Global OFT) or combined with local block matching refinement [45] are also presented. Note that, since these methodologies share the segmentation algorithm applied to the ED frame, they present the same results for the ED metrics and indices. Overall, the proposed localized strategy presented similar distance metrics, with smaller bias and limits of agreement for both ESV and EF. In Figure 8, two example segmentation (at the ED frame) and tracking (at the ES frame) results are illustrated, with corresponding absolute distance errors mapped on the LV endocardial surface. The largest errors were found at the apex, with some segments of the LV base (mostly at the lateral wall) also presenting slightly higher distances to the

Table I. Performance on the CETUS database for mean absolute distance (MAD), Hausdorff distance (HD) and Dice coefficient (Dice). State-of-the-art approaches are also presented.

Method	**MAD** (mm)		**HD** (mm)		**Dice**	
	ED	**ES**	**ED**	**ES**	**ED**	**ES**
Proposed	2.26±0.72	2.45±0.85	8.10±2.62	8.29±3.01	0.894±0.040	0.861±0.054
Global OFT	2.26±0.72	2.41±0.87	8.10±2.62	8.13±2.97	0.894±0.040	0.858±0.056
[45]	2.26±0.72	2.43±0.89	8.10±2.62	8.13±3.03	0.894±0.040	0.856±0.056
[17]	2.37±x.xx	2.64±x.xx	9.41±x.xx	9.34±x.xx	0.882±x.xx	0.837±x.xx
[21]	1.91±x.xx	2.48±x.xx	6.66±x.xx	7.38±x.xx	0.910±x.xx	0.862±x.xx
[23]	2.18±0.70	2.47±0.74	7.55±1.76	8.57±2.96	0.894±0.030	0.849±0.040
[24]	1.94±0.55	2.23±0.60	7.00±1.99	7.53±2.23	0.904±0.020	0.874±0.040

Table II. Performance on the CETUS database for Pearson's correlation coefficient (R) and Bland-Altman LOA ($\mu \pm \sigma$) between automatic and reference LV cardiac indices (EDV, ESV and EF). State-of-the-art approaches are also presented.

Method	**EDV** (ml)		**ESV** (ml)		**EF** (%)		**Score**
	R	**LOA**	**R**	**LOA**	**R**	**LOA**	
Proposed	0.965	-4.99±17.66	0.971	-5.83^a±13.14	0.927	2.30±4.20	0.623
Global OFT	0.965	-4.99±17.66	0.968	-6.40^a±13.69	0.894	2.70±5.10	0.638
[45]	0.965	-4.99±17.66	0.967	-6.78^a±13.86	0.889	2.88±5.24	0.644
[17]	0.979	2.74±13.87	0.968	2.18±13.73	0.811	0.05±7.84	0.666
[21]	0.958	-4.86±18.08	0.965	-15.39±15.08	0.751	8.40±7.72	0.694
[23]	0.945	-6.02±20.82	0.924	-0.42±20.62	0.780	-1.55±6.94	0.719
[24]	0.961	-4.14±17.35	0.973	-3.47±13.62	0.892	0.48±5.50	-

$^a p < 0.05$, two-tailed paired t-test against zero.

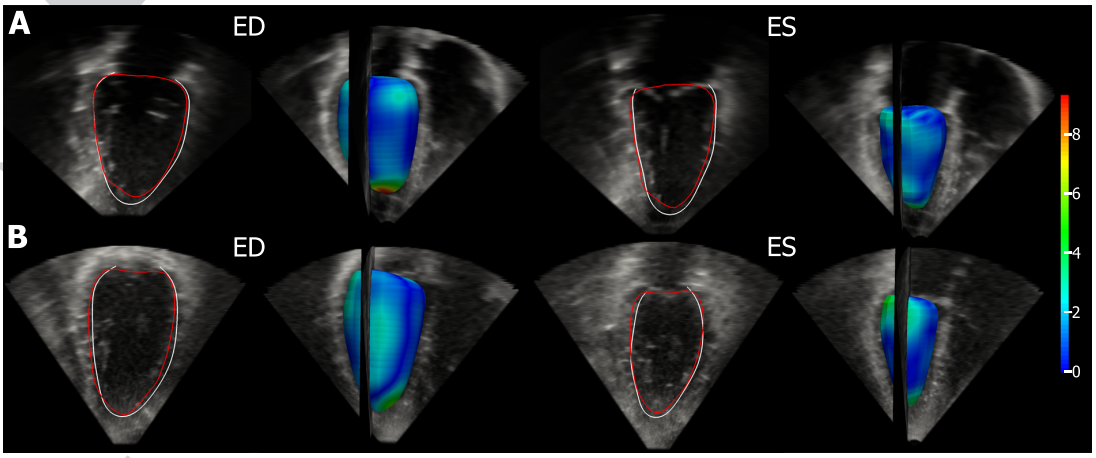

Figure 8. Segmentation plus tracking result for two representative example 3D US datasets of the CETUS database (white: ground truth; red: automatic endocardial surface). The colored surface represents the resulting LV surface at ED and ES frames mapped with corresponding absolute distance errors.

reference mesh. Note, however, that the highest errors seen at the apex are also related to the largest error already present at the ED phase and related to the original automatic LV segmentation [45].

Regarding its computational burden, the proposed methodology took, on average, 0.8 s/frame. Note that a smaller average computational time was found compared to the previous experiment (Section 3.1.4) due to the smaller radius (in pixels) used for the neighboring regions (*i.e.* larger voxel spacing of the clinical datasets compared to the simulated ones).

3.3. Cine cardiac magnetic resonance

3.3.1. Data description: To demonstrate the multi-modality feature of the proposed localized tracking strategy, this third experiment focuses on validating the method's applicability on cine CMR datasets from the 2009 MICCAI CMR LV segmentation challenge[§] [53]. The database includes 45 cine steady state free precession pulse sequences. Six to twelve images were obtained from the atrioventricular ring to the apex, with a temporal resolution of 20 phases over the cardiac cycle and an isotropic pixel spacing ranging from 1.29 to 1.56 mm. The challenge's population includes 36 patients (12 with heart failure and myocardial infarction, 12 with heart failure but no myocardial infarction and 12 with hypertrophic cardiomyopathy) and 9 healthy subjects. Moreover, ground truth borders drawn by an experienced observer are available in all slices for both endo- and epicardium at the ED phase and for the endocardium at the ES phase. All results consider manual contours drawn to include trabeculae and papillary muscles in the LV cavity.

3.3.2. Implementation details: In this final experiment, we propose to assess the performance of the proposed tracking methodology when combined with a previously presented LV segmentation framework for 4D cine CMR datasets [16]. The original framework delineates the myocardial boundaries at all frames in a three-step approach: (1) automatic initialization and segmentation of the LV myocardium in an ED mid-ventricular short-axis slice; (2) automatic 3D myocardial segmentation at the ED phase; and (3) tracking of the ED contours throughout the full sequence using the global anatomically constrained affine optical flow strategy. While the framework presented highly competitive results against state-of-the-art methods and excellent correlations with reference cardiac indices [16], the third module was found to be the least performing one. Hereto, we propose to replace the third module by our localized tracking strategy, propagating the automatically segmented ED LV surfaces by locally estimating the motion between adjacent cardiac phases. Similarly to Queirós *et al.* [16] and due to the anisotropy of the CMR data, such estimation is performed independently for each slice sequence and for each myocardial boundary. The present implementation corresponds to a particular case of the 3D mathematical formalism described in Section 2. Indeed, such slice-based tracking can be described based on a cylindrical space, $\Gamma(\theta, z)$, in which the second localized support parameter is given by $\sigma_z = \delta$.

In the present CMR database, σ_θ was set to $3\pi/8$ rad, with 4 iterations on the refinement scheme and a 1 px SD on the Gaussian derivative kernels. Since a slice-based tracking is intended, a squared neighborhood function was used, with $[7 \times 7]$ px (leading to $\sim 9 - 10$ mm).

[§]https://www.cardiacatlas.org/

Table III. Performance on the 45 CMR datasets, in terms of average perpendicular distance (APD), Hausdorff distance (HD), Dice coefficient (Dice) and percentage of good contours.

Method	**APD** (mm)		**HD** (mm)		**Dice**		**Good contours** (%)	
	Endo	**Epi**	**Endo**	**Epi**	**Endo**	**Epi**	**Endo**	**Epi**
Proposed	2.07±0.84	2.06±0.84	5.14±1.88	5.14±1.79	0.88±0.06	0.93±0.03	94.3±8.5	95.4±9.6
[16]	2.14±0.88[a]		5.05±1.85[a]		0.87±0.07[a]		92.7±9.5	

[a] $p < 0.05$, paired t-test against proposed method.

Table IV. Performance on the 45 CMR datasets, in terms of Pearson's correlation coefficient (R) and Bland-Altman LOA ($\mu \pm \sigma$) between automatic and reference LV cardiac indices (EDV, ESV, SV, LVM and EF).

Method	**EDV** (ml)		**ESV** (ml)		**SV** (ml)		**LVM** (g)		**EF** (%)	
	R	**LOA**	**R**	**LOA**	**R**	**LOA**	**R**	**LOA**	**R**	**LOA**
Proposed	0.985	-2.46±15.03	0.989	-2.75±13.66	0.962	0.30±7.71	0.951	5.51[a]±14.13	0.980	1.87[a]±4.54
[16]			0.988	-3.83[b]±14.78	0.955	1.38[b]±8.07			0.976	3.00[a,b]±5.60

[a] $p < 0.05$, two-tailed paired t-test against zero.
[b] $p < 0.05$, two-tailed paired t-test against proposed method.
No statistically significant differences were found on a two-tailed F-test between methods.

3.3.3. Performance assessment: The performance of the proposed algorithm (segmentation plus tracking combined) was assessed using distance metrics and LV clinical indices against reference surfaces and indices, respectively. The percentage of good contours (average perpendicular distance < 5 mm) was also computed, as advised by the challenge's organizers [53]. Note that epicardial results are unchanged since no expert delineations are available at the ES phase (as only endocardial surface is needed for cardiac indices computation). Finally, the results were compared against the global tracking methodology. A two-tailed paired t-test and a F-test were used to check for statistically significant differences in their biases and LOAs, respectively. Our null hypothesis was that no difference exists, and p-values < 0.05 were considered statistically significant.

3.3.4. Results: Table III and Table IV summarize the overall segmentation plus tracking performance for the 45 CMR datasets. The results for the original framework are also included for comparative purposes. Moreover, Figure 9 presents one tracking example for a mid-ventricular CMR slice. Overall, both APD and Dice metrics significantly improved when using the proposed localized tracking strategy, while statistically significant improvements were also found for all parameters that depend on the tracking module (*i.e.* ESV, SV and EF). Specifically, all biases were significantly reduced, while a tendency for smaller LOAs were observed, particularly for EF. The localized tracking took, on average, 0.015 s/slice, which represents roughly 0.12 s/frame. The smaller computational time in comparison to previous experiments is directly related to the slice-based tracking since only 2D neighbor regions are used, greatly reducing its computational burden.

4. DISCUSSION

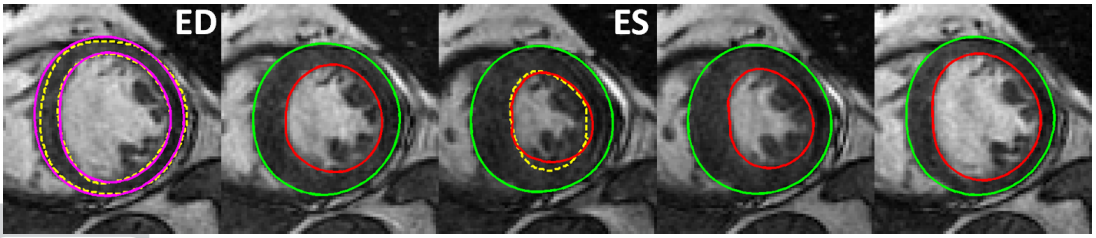

Figure 9. Localized tracking result for one mid-ventricular slice of a CMR dataset (magenta: automatic contour at the ED phase; red: tracked endocardium; green: tracked epicardium; yellow: ground truth).

In this work, a novel fast and automatic methodology based on localized anatomically constrained affine optical flow is proposed for left ventricle tracking in multiple imaging modalities. The methodology was validated in three distinct public databases, focusing on assessing its feasibility and accuracy for global and regional LV function assessment.

The proposed method showed excellent global tracking performance in the realistically simulated US sequences (Figure 4). By performing an independent localized motion estimation for each target surface point, contrarily to the original global affine model, the proposed method clearly increases the degrees of freedom to capture local myocardial motion (see Figure 2E-F). Indeed, when compared to its global counterpart, the localized tracking strategy showed to be able to better capture local heterogeneity in myocardial motion and deformation (Figure 3 and Figure 5), without however losing spatial consistency (Figure 4 and Figure 8). Note that a similar accuracy improvement was obtained for the 15 training datasets of the clinical data when assessing the tracking algorithm only (Figure 7). Such improved performance is most relevant in pathological cases (*i.e.* patients with pathophysiological conditions affecting myocardial deformation), as is the case of the synthetic sequences used for this validation. Importantly, note that in opposition to other methods that regularize a motion field estimated *a priori* (based on anatomical or functional assumptions) [28, 33, 40], the proposed approach embeds the anatomical information (through a local affine motion model constrained to an anatomical ROI) directly into the optical flow computation. Therefore, a more efficient framework is obtained, without also depending on the accuracy of a preceding motion estimation step.

When assessing tracking accuracy throughout the cardiac cycle (Figure 5C), the largest errors were found at the ES time point. This is mainly related to the largest myocardial displacements at this stage, which is simultaneously the limitation of traditional optical flow strategies [34]. Nonetheless, the use of an iterative refinement scheme together with a bi-directional tracking strategy allowed to reduce overall error accumulation and still largely capture the myocardial motion (Figure 5C, note that the average displacement at ES is nearly 5 mm). When considering the 3 myocardial layers separately (Figure 5D), the highest errors were found at the epicardium. Such result is mostly associated to the poorer delineation of its borders on cardiac ultrasound [8], which reduces the

visual cues available to be tracked using our differential optical flow method. Moreover, looking to their spatial distribution, the highest errors were located in the lateral wall, probably related to the commonly found artifacts in this region, such as out-of-field effects and surrounding structures interferences [54]. Finally, when considering apical, mid-ventricular and basal levels, the latter generally presented higher errors (Figure 5B). Nonetheless, for this particular experiment, such result might be, in part, associated to the open surface available at the ED frame. Indeed, the use of mirror boundary conditions at the LV base does not entirely reproduce what is physiologically expectable. Moreover, the perceptible movement associated to the cardiac valves (and simulated in these datasets) might also affect the tracking accuracy at this level.

Notably, the sensitivity analysis on 4 important hyper-parameters (Figure 3) revealed that the overall performance is not significantly impaired within a fairly large range of parameters settings. The localized support parameters, σ_θ and σ_φ, were the only ones leading to a statistically significant reduction on the performance within the studied range, and only for a variation of $+50\%$. This result is probably related to a smoother (*i.e.* more globalized) tracking at this extreme variation, which decreases its accuracy for capturing local motion patterns, namely on the ischemic dataset. It is important to note that such parameters allow to choose from a single neighbor region estimation (less robust and resulting in a more irregular tracking) to a full global support estimation (as in its global counterpart, being robust but less capable of local deformation capture). Therefore, a trade-off between robustness and localized estimation exists when setting these parameters, which should be done according to the application and target structure. Regarding the number of iterations used in the refinement scheme, although no statistically significant differences were found, a performance improvement is seen with an increase in this parameter. Nonetheless, one should note that the method's computational burden is directly proportional to it. Thus, according to the expected amount of motion of the target structure, this parameter should be set to allow for accurate results and, preferentially, minimal computational burden. The last two parameters (n_{nhood} and σ_{g_kernel}) did not present any marked tendency within the studied range. As for the number of iterations, note that a larger radius on the cubic neighbor region has a significant impact on the method's computational time. Again, it should be set to capture enough boundary information to track the target, but small enough to avoid interference from surrounding tissues and to keep it computationally efficient.

Concerning strain estimation (Figure 6), the automatically obtained strain maps for the localized AAOF strategy were found to be qualitatively similar to the ground truth (which was not observed for the global counterpart), proving the method's feasibility for regional LV function assessment. Due to the method's localized support, all strain maps presented smoother displacements compared to reference ones. When looking to each anatomical direction independently, the proposed method presented an accurate quantification of the longitudinal strain, a slight underestimation of the

circumferential strain and an overestimation of the radial strain. Nevertheless, ischemic segments could still be easily identified by lower (absolute) strain values (e.g., see circumferential strain in Figure 6) using the proposed method. Note that the lower accuracy for the radial direction is common for deformation assessment in 3D US [41], with higher deformations being expected in this direction. Moreover, it might also be linked to the fact that no constraints were added in this direction (*i.e.* not directly affected by the chosen localized support parameters), with an independent propagation being applied for each myocardial layer. Such result could be improved by the use of explicit constraints, such as the assumption of myocardial volume conservation [29], or by a post-processing regularization step [33, 40].

In the clinical experiments (Section 3.2 and 3.3), the proposed tracking strategy when combined to previously presented automatic segmentation strategies [16, 45] proved to improve performance in both 3D US (Table I and Table II) and cine CMR datasets (Table III and Table IV). Both original methods are state-of-the-art strategies with leading results on both accuracy and computational time on their respective databases [16, 45]. Nevertheless, both used the global counterpart of the proposed method, which was found to be their limitation module. Indeed, to increase its accuracy for localized LV tracking, a local refinement scheme based on block matching had already been presented for 3D US [45]. However, the proposed localized anatomically constrained optical flow presented an improved performance, with smaller biases, narrower limits of agreement (namely of near 20% for the EF) and higher correlations to reference cardiac indices (Table II), ultimately obtaining a better score on the CETUS database. In fact, the proposed approach outperformed other state-of-the-art approaches (namely higher correlations and narrower LOAs for ESV and EF) [17, 21, 23], with the largest score (*i.e.* lower value) in the current challenge ranking. When assessing the spatial distribution of the errors (Figure 8), similarly to the simulated US datasets, the largest errors were found in some segments of the LV base (mostly at the lateral wall), but also at the apex region. Note, however, that the latter is generally related to the largest errors already present at the ED phase and related to the automatic segmentation framework. Such dependency on the initial surface demonstrates the importance of combining our tracking strategy with an accurate initial segmentation strategy. The same improved results were observed in cine CMR datasets (namely $\sim$ 20% reduction in the LOA for EF), with simultaneous statistically significant improvement on the distance metrics (namely, APD and Dice). Note, nonetheless, that the tracking accuracy is still limited by the interaction between the papillary muscles and the myocardium throughout the contraction phase, being this one of the main source of errors. Overall, the localized tracking strategy showed an improved accuracy compared to its global counterpart on both modalities (which were leading results in their respective public databases), while simultaneously providing a feasible method for regional function assessment.

Finally, the proposed methodology proved to be viable for online processing, showing to be computationally efficient in all 3 experiments. As mentioned above, the number of iterations and the size of the neighbor region used for the optical flow estimation were found to be the main hyper-parameters controlling the method's computational burden. When compared to other state-of-the-art methods (e.g., surface-based tracking [38], non-rigid registration [30, 32] or block matching [28] approaches, among others [41]), the proposed method was found to be competitive in terms of computational time, which is paramount for success in daily cardiology practice.

Importantly, although here presented for multi-modality LV tracking, the proposed localized anatomically constrained affine optical flow is applicable to many other target structures (e.g., other cardiac chambers, valves or even other organs). As mentioned in Section 2, the choice of an appropriate coordinate space together with the localized support parameters can provide implicit anatomical priors for an accurate tracking. For example, consider the case of a tube-like structure (e.g., aortic root wall) in which a larger motion occurs along the radial direction (with higher variation between different portions of the wall) than along the longitudinal one. In this case, a cylindrical space could be used, in which a smaller value would be given to σ_θ, thus increasing the degrees of freedom to capture larger localized deformations, and a higher value would be set to σ_z, increasing the robustness against image artifacts or other misleading image information. The same rationale could be used for other applications, with suitable hyper-parameters having to be set to achieve an accurate surface tracking, and ultimately assess the target's global and regional motion/deformation. Moreover, the proposed strategy could be used as input to other algorithms in order to create patient-specific LV models and study the onset of specific cardiac diseases [55, 56, 57, 58].

5. CONCLUSION

In this work, a novel fast and automatic left ventricle tracking methodology based on localized anatomically constrained affine optical flow is proposed. The methodology's feasibility and accuracy for global and regional myocardial function assessment was evaluated in three distinct databases, achieving accurate tracking results in all. Experiments on realistically simulated 3D US data showed the method's applicability and accuracy for global and regional function assessment. When combined with state-of-the-art segmentation strategies, the method proved to be robust for LV surface tracking throughout the cardiac cycle in both 3D echocardiography and cine CMR data. Its results outperformed the original global formulation, with smaller biases and narrower limits of agreement for the relevant clinical cardiac indices, while providing a feasible strategy for regional

function assessment. Finally, the proposed localized tracking method showed to be suitable for online processing, being a critical factor for success in clinical practice.

ACKNOWLEDGEMENTS

The authors acknowledge funding support from FCT - Fundação para a Ciência e a Tecnologia, Portugal, and the European Social Found, European Union, through the Programa Operacional Capital Humano (POCH) in the scope of the PhD grants SFRH/BD/93443/2013 (S. Queirós) and SFRH/BD/95438/2013 (P. Morais), and by the project 'PersonalizedNOS (01-0145-FEDER-000013)' co-funded by *Programa Operacional Regional do Norte* (Norte2020) through the European Regional Development Fund (ERDF).

REFERENCES

1. Elliott PM, Anastasakis A, Borger MA, Borggrefe M, Cecchi F, Charron P, Hagege AA, Lafont A, Limongelli G, Mahrholdt H, *et al.*. 2014 ESC guidelines on diagnosis and management of hypertrophic cardiomyopathy. *European Heart Journal* 2014; **35**(39):2733–2779.
2. Vahanian A, Alfieri O, Andreotti F, Antunes MJ, Barón-Esquivias G, Baumgartner H, Borger MA, Carrel TP, De Bonis M, Evangelista A, *et al.*. Guidelines on the management of valvular heart disease (version 2012). *European heart journal* 2012; **33**(19):2451–2496.
3. Yancy CW, Jessup M, Bozkurt B, Butler J, Casey DE, Drazner MH, Fonarow GC, Geraci SA, Horwich T, Januzzi JL, *et al.*. 2013 ACCF/AHA guideline for the management of heart failure: a report of the American College of Cardiology Foundation/American Heart Association Task Force on practice guidelines. *Journal of the American College of Cardiology* 2013; **62**(16):e147–e239.
4. Lang RM, Badano LP, Mor-Avi V, Afilalo J, Armstrong A, Ernande L, Flachskampf FA, Foster E, Goldstein SA, Kuznetsova T, *et al.*. Recommendations for cardiac chamber quantification by echocardiography in adults: An update from the American Society of Echocardiography and the European Association of Cardiovascular Imaging. *European Heart Journal - Cardiovascular Imaging* 2015; **16**(3):233–271.
5. Miller CA, Jordan P, Borg A, Argyle R, Clark D, Pearce K, Schmitt M. Quantification of left ventricular indices from SSFP cine imaging: Impact of real-world variability in analysis methodology and utility of geometric modeling. *Journal of Magnetic Resonance Imaging* 2013; **37**(5):1213–1222.
6. Jasaityte R, Heyde B, Dhooge J. Current state of three-dimensional myocardial strain estimation using echocardiography. *Journal of the American Society of Echocardiography* 2013; **26**(1):15–28.
7. Petitjean C, Dacher JN. A review of segmentation methods in short axis cardiac MR images. *Medical image analysis* 2011; **15**(2):169–184.
8. Noble JA, Boukerroui D. Ultrasound image segmentation: a survey. *IEEE Transactions on Medical Imaging* 2006; **25**(8):987–1010.
9. Hu H, Liu H, Gao Z, Huang L. Hybrid segmentation of left ventricle in cardiac MRI using gaussian-mixture model and region restricted dynamic programming. *Magnetic resonance imaging* 2013; **31**(4):575–584.
10. Cordero-Grande L, Vegas-Sánchez-Ferrero G, Casaseca-de-la Higuera P, San-Román-Calvar JA, Revilla-Orodea A, Martín-Fernández M, Alberola-López C. Unsupervised 4D myocardium segmentation with a Markov Random Field based deformable model. *Medical image analysis* 2011; **15**(3):283–301.
11. Lynch M, Ghita O, Whelan PF. Segmentation of the left ventricle of the heart in 3-D+t MRI data using an optimized nonrigid temporal model. *IEEE Transactions on Medical Imaging* 2008; **27**(2):195–203.

12. Ben Ayed I, Li S, Ross I. Embedding overlap priors in variational left ventricle tracking. *IEEE Transactions on Medical Imaging* 2009; **28**(12):1902–1913.
13. Dakua SP, Sahambi J. Modified active contour model and random walk approach for left ventricular cardiac MR image segmentation. *International Journal for Numerical Methods in Biomedical Engineering* 2011; **27**(9):1350–1361.
14. Dietenbeck T, Alessandrini M, Barbosa D, Dhooge J, Friboulet D, Bernard O. Detection of the whole myocardium in 2D-echocardiography for multiple orientations using a geometrically constrained level-set. *Medical image analysis* 2012; **16**(2):386–401.
15. Barbosa D, Dietenbeck T, Heyde B, Houle H, Friboulet D, D'hooge J, Bernard O. Fast and fully automatic 3-d echocardiographic segmentation using B-spline explicit active surfaces: Feasibility study and validation in a clinical setting. *Ultrasound in medicine & biology* 2013; **39**(1):89–101.
16. Queirós S, Barbosa D, Heyde B, Morais P, Vilaça JL, Friboulet D, Bernard O, D'hooge J. Fast automatic myocardial segmentation in 4D cine CMR datasets. *Medical image analysis* 2014; **18**(7):1115–1131.
17. Bernier M, Jodoin P, Lalande A. Automatized evaluation of the left ventricular ejection fraction from echocardiographic images using graph cut. *Proceedings of the MICCAI Challenge on Endocardial Three-dimensional Ultrasound Segmentation (CETUS)* 2014; :25–32.
18. Zhang H, Wahle A, Johnson RK, Scholz TD, Sonka M. 4-D cardiac MR image analysis: left and right ventricular morphology and function. *IEEE Transactions on Medical Imaging* 2010; **29**(2):350–364.
19. Mitchell SC, Bosch JG, Lelieveldt BP, Van der Geest RJ, Reiber JH, Sonka M. 3-D active appearance models: segmentation of cardiac MR and ultrasound images. *IEEE Transactions on Medical Imaging* 2002; **21**(9):1167–1178.
20. Haak A, Vegas-Sanchez-Ferrero G, Mulder HW, Ren B, Metz C, van Burken G, van Stralen M, Pluim JP, van der Steen F, van Walsum T, *et al.*. Segmentation of multiple heart cavities in 3-D transesophageal ultrasound images. *IEEE Transactions on Ultrasonics, Ferroelectrics, and Frequency Control* 2015; **62**(6):1179–1189.
21. van Stralen M, Haak A, Leung KE, van Burken G, Bos C, Bosch JG. Full-cycle left ventricular segmentation and tracking in 3d echocardiography using active appearance models. *2015 IEEE International Ultrasonics Symposium (IUS)*, IEEE, 2015; 1–4.
22. Zhuang X, Rhode KS, Razavi RS, Hawkes DJ, Ourselin S. A registration-based propagation framework for automatic whole heart segmentation of cardiac MRI. *IEEE Transactions on Medical Imaging* 2010; **29**(9):1612–1625.
23. Oktay O, Shi W, Keraudren K, Caballero J, Rueckert D, Hajnal J. Learning shape representations for multi-atlas endocardium segmentation in 3d echo images. *Proceedings of the MICCAI Challenge on Endocardial Three-dimensional Ultrasound Segmentation (CETUS)* 2014; :57–64.
24. Oktay O, Gomez A, Keraudren K, Schuh A, Bai W, Shi W, Penney G, Rueckert D. Probabilistic edge map (PEM) for 3D ultrasound image registration and multi-atlas left ventricle segmentation. *Functional Imaging and Modeling of the Heart*. Springer, 2015; 223–230.
25. Yang L, Georgescu B, Zheng Y, Meer P, Comaniciu D. 3D ultrasound tracking of the left ventricle using one-step forward prediction and data fusion of collaborative trackers. *IEEE Conference on Computer Vision and Pattern Recognition, 2008*, IEEE, 2008; 1–8.
26. Zheng Y, Barbu A, Georgescu B, Scheuering M, Comaniciu D. Four-chamber heart modeling and automatic segmentation for 3-D cardiac CT volumes using marginal space learning and steerable features. *IEEE Transactions on Medical Imaging* 2008; **27**(11):1668–1681.
27. Lu X, Wang Y, Georgescu B, Littman A, Comaniciu D. Automatic delineation of left and right ventricles in cardiac MRI sequences using a joint ventricular model. *Functional Imaging and Modeling of the Heart*. Springer, 2011; 250–258.

28. Crosby J, Amundsen BH, Hergum T, Remme EW, Langeland S, Torp H. 3-D speckle tracking for assessment of regional left ventricular function. *Ultrasound in medicine & biology* 2009; **35**(3):458–471.
29. Heyde B, Alessandrini M, Hermans J, Barbosa D, Claus P, D'hooge J. Anatomical image registration using volume conservation to assess cardiac deformation from 3D ultrasound recordings. *IEEE Transactions on Medical Imaging* 2015; **PP**(99):1–1.
30. Elen A, Choi HF, Loeckx D, Gao H, Claus P, Suetens P, Maes F, Hooge JD. Three-dimensional cardiac strain estimation using spatio–temporal elastic registration of ultrasound images: A feasibility study. *IEEE Transactions on Medical Imaging* 2008; **27**(11):1580–1591.
31. Heyde B, Bouchez S, Thieren S, Vandenheuvel M, Jasaityte R, Barbosa D, Claus P, Maes F, Wouters P, D'hooge J. Elastic image registration to quantify 3-D regional myocardial deformation from volumetric ultrasound: experimental validation in an animal model. *Ultrasound in medicine & biology* 2013; **39**(9):1688–1697.
32. De Craene M, Piella G, Camara O, Duchateau N, Silva E, Doltra A, Dhooge J, Brugada J, Sitges M, Frangi AF. Temporal diffeomorphic free-form deformation: Application to motion and strain estimation from 3D echocardiography. *Medical Image Analysis* 2012; **16**(2):427–450.
33. McLeod K, Sermesant M, Beerbaum P, Pennec X. Spatio-temporal tensor decomposition of a polyaffine motion model for a better analysis of pathological left ventricular dynamics. *Medical Imaging, IEEE Transactions on* 2015; **34**(7):1562–1575.
34. Barbosa D, Heyde B, Dietenbeck T, Friboulet D, D'hooge J, Bernard O. Fast left ventricle tracking in 3D echocardiographic data using anatomical affine optical flow. *Functional Imaging and Modeling of the Heart*. Springer, 2013; 191–199.
35. Alessandrini M, Liebgott H, Barbosa D, Bernard O. Monogenic phase based optical flow computation for myocardial motion analysis in 3D echocardiography. *Statistical Atlases and Computational Models of the Heart. Imaging and Modelling Challenges*, *Lecture Notes in Computer Science*, vol. 7746, Camara O, Mansi T, Pop M, Rhode K, Sermesant M, Young A (eds.). Springer Berlin Heidelberg, 2013; 159–168.
36. Mukherjee R, Sprouse C, Pinheiro A, Abraham T, Burlina P. Computing myocardial motion in 4-dimensional echocardiography. *Ultrasound in medicine & biology* 2012; **38**(7):1284–1297.
37. Xavier M, Lalande A, Walker PM, Brunotte F, Legrand L. An adapted optical flow algorithm for robust quantification of cardiac wall motion from standard cine-MR examinations. *IEEE Transactions on Information Technology in Biomedicine* 2012; **16**(5):859–868.
38. Hautvast G, Lobregt S, Breeuwer M, Gerritsen F. Automatic contour propagation in cine cardiac magnetic resonance images. *IEEE Transactions on Medical Imaging* 2006; **25**(11):1472–1482.
39. Yang L, Georgescu B, Zheng Y, Wang Y, Meer P, Comaniciu D. Prediction based collaborative trackers (PCT): A robust and accurate approach toward 3D medical object tracking. *IEEE Transactions on Medical Imaging* 2011; **30**(11):1921–1932.
40. Zhou Y, Bernard O, Saloux E, Manrique A, Allain P, Makram-Ebeid S, De Craene M. 3d harmonic phase tracking with anatomical regularization. *Medical Image Analysis* 2015; **26**(1):70–81.
41. De Craene M, Marchesseau S, Heyde B, Gao H, Alessandrini M, Bernard O, Piella G, Porras AR, Tautz L, Hennemuth A, *et al.*. 3D strain assessment in ultrasound (straus): A synthetic comparison of five tracking methodologies. *IEEE Transactions on Medical Imaging* 2013; **32**(9):1632–1646.
42. Motto A. Three-dimensional echocardiography for optimization of cardiac resynchronization therapy. *European Heart Journal* 2009; **30**:505–508.
43. Barbosa D, Dietenbeck T, Schaerer J, D'hooge J, Friboulet D, Bernard O. B-spline explicit active surfaces: an efficient framework for real-time 3-D region-based segmentation. *IEEE Transactions on Image Processing* 2012; **21**(1):241–251.
44. Queirós S, Vilaça JL, Morais P, Fonseca JC, D'hooge J, Barbosa D. Fast left ventricle tracking in CMR images using localized anatomical affine optical flow. *SPIE Medical Imaging*, International Society for Optics and Photonics,

2015; 941 306–941 306.

45. Barbosa D, Friboulet D, D'hooge J, Bernard O. Fast tracking of the left ventricle using global anatomical affine optical flow and local recursive block matching. *Proceedings of the MICCAI Challenge on Endocardial Three-dimensional Ultrasound Segmentation (CETUS)*, 2014.
46. Lucas BD, Kanade T. An iterative image registration technique with an application to stereo vision. *Proceedings of the 7th International Joint Conference on Artificial Intelligence - Volume 2*, IJCAI'81, Morgan Kaufmann Publishers Inc.: San Francisco, CA, USA, 1981; 674–679.
47. Sühling M, Arigovindan M, Hunziker P, Unser M. Multiresolution moment filters: Theory and applications. *Image Processing, IEEE Transactions on* 2004; **13**(4):484–495.
48. Alessandrini M, De Craene M, Bernard O, Giffard-Roisin S, Allain P, Waechter-Stehle I, Weese J, Saloux E, Delingette H, Sermesant M, *et al.*. A pipeline for the generation of realistic 3D synthetic echocardiographic sequences: Methodology and open-access database. *IEEE Transactions on Medical Imaging* July 2015; **34**(7):1436–1451.
49. Cerqueira MD, Weissman NJ, Dilsizian V, Jacobs AK, Kaul S, Laskey WK, Pennell DJ, Rumberger JA, Ryan T, Verani MS, *et al.*. Standardized myocardial segmentation and nomenclature for tomographic imaging of the heart a statement for healthcare professionals from the cardiac imaging committee of the Council on Clinical Cardiology of the American Heart Association. *Circulation* 2002; **105**(4):539–542.
50. Bernard O, Bosch JG, Heyde B, Alessandrini M, Barbosa D, Camarasu-Pop S, Cervenansky F, Valette S, Mirea O, Bernier M, *et al.*. Standardized evaluation system for left ventricular segmentation algorithms in 3d echocardiography. *IEEE Transactions on Medical Imaging* 2016; **35**(4):967–977.
51. Papachristidis A, Geleijnse M, Galli E, Heyde B, Alessandrini M, Barbosa D, Donal E, Monaghan M, Bernard O, D'hooge J, *et al.*. Clinical expert delineation of 3D left ventricular echocardiograms for the CETUS segmentation challenge. *Proceedings of the MICCAI Challenge on Endocardial Three-dimensional Ultrasound Segmentation (CETUS)* 2014; :9–16.
52. Bland JM, Altman D. Statistical methods for assessing agreement between two methods of clinical measurement. *The lancet* 1986; **327**(8476):307–310.
53. Radau P, Lu Y, Connelly K, Paul G, Dick A, Wright G. Evaluation framework for algorithms segmenting short axis cardiac MRI. *The MIDAS Journal - Cardiac MR Left Ventricle Segmentation Challenge* 2009; **49**.
54. Tobon-Gomez C, De Craene M, Mcleod K, Tautz L, Shi W, Hennemuth A, Prakosa A, Wang H, Carr-White G, Kapetanakis S, *et al.*. Benchmarking framework for myocardial tracking and deformation algorithms: An open access database. *Medical Image Analysis* 2013; **17**(6):632–648.
55. Gao H, Wang H, Berry C, Luo X, Griffith BE. Quasi-static image-based immersed boundary-finite element model of left ventricle under diastolic loading. *International journal for numerical methods in biomedical engineering* 2014; **30**(11):1199–1222.
56. Hadjicharalambous M, Asner L, Chabiniok R, Sammut E, Wong J, Peressutti D, Kerfoot E, King A, Lee J, Razavi R, *et al.*. Non-invasive model-based assessment of passive left-ventricular myocardial stiffness in healthy subjects and in patients with non-ischemic dilated cardiomyopathy. *Annals of Biomedical Engineering* 2016; :1–14.
57. Evangelista A, Gabriele S, Nardinocchi P, Piras P, Puddu P, Teresi L, Torromeo C, Varano V. A comparative analysis of the strain-line pattern in the human left ventricle: experiments vs modelling. *Computer Methods in Biomechanics and Biomedical Engineering: Imaging & Visualization* 2016; **4**(3-4):164–173.
58. de Vecchi A, Gomez A, Pushparajah K, Schaeffter T, Simpson J, Razavi R, Penney G, Smith N, Nordsletten D. A novel methodology for personalized simulations of ventricular hemodynamics from noninvasive imaging data. *Computerized Medical Imaging and Graphics* 2016; **51**:20–31.